Trailed Circulation of Hovering Rotors with Leading-Edge Protuberances

Brian Cully,* Joseph I. Milluzzo III,† and Scott Drayton‡

U.S. Naval Academy Rotorcraft Center, Annapolis, MD, 21402

ABSTRACT

The effect of leading-edge protuberances on the wake of a rotor hovering out of ground effect was examined using performance and phase-resolved particle image velocimetry measurements. Protuberance amplitude and wavelength were investigated using a set of baseline rectangular blades and four blade sets with various sinusoidal leading-edges. For blade loading coefficients below 0.06, protuberances had minimal effect on rotor performance, but as the thrust increased the modified blades began to incur an additional power requirement. The rotor wake was significantly affected by protuberance amplitude. Specifically, increasing protuberance amplitude generated a more uniform inflow distribution, as well as increased size, magnitude, and strength of the vorticity trailed into the wake sheet. Furthermore, an examination of the spanwise distribution of circulation trailed into the wake sheets showed that the modified blades produced a sinusoidal variation in both the positive and negative circulation distribution. As compared to the baseline blade, the highest amplitude blades also increased the magnitude of the mean circulation (both positive and negative) about which the sinusoidal oscillation occurred.

NOMENCLATURE

A	Disk area, m^2
A_b	Blade area, m^2
c	Blade chord, m
C_P	Rotor power coefficient, $= P/\rho\pi\Omega^3R^5$
C_{P_0}	Rotor profile power coefficient, $= P_0/\rho\pi\Omega^3R^5$
C_{P_i}	Rotor Induced power coefficient, $= \kappa C_{P_{\text{ideal}}}$
$C_{P_{\text{ideal}}}$	Ideal power coefficient, $= C_T^{3/2}/\sqrt{2}$
C_T	Rotor thrust coefficient, $= T/\rho\pi\Omega^2R^4$
C_P/σ	Power loading coefficient
C_T/σ	Blade loading coefficient
FM	Figure of merit, $= P_{\text{ideal}}/P_{\text{measured}}$
N_b	Number of blades
R	Radius of blade, m
r	Radial distance, m
T	Rotor thrust, N
u, v	Velocities in the r and z directions, $\mathrm{m\,s}^{-1}$
v_i	Induced velocity, $\mathrm{m\,s}^{-1}$
V_{tip}	Rotor tip speed, $= \Omega R$, $\mathrm{m\,s}^{-1}$
z	Distance from rotor plane, m
ζ	Wake age, deg
θ_{TW}	Twist rate, deg
κ	Induced power factor
λ	Inflow ratio, $= v_i/V_{\text{tip}}$
ρ	Flow density, $\mathrm{kg\,m}^{-3}$
σ	Rotor solidity, $= A_b/A$
σ_e	Thrust-weighted rotor solidity, $= 3\int_0^1 \sigma(r)r^2dr$
ψ_b	Blade azimuth position, deg
Ω	Rotational speed of the rotor, s^{-1}
ω	Vorticity, s^{-1}

*Ensign, United States Navy, bpcully@gmail.com

†Assistant Professor, Department of Aerospace Engineering, 332A Rickover Hall; milluzzo@usna.edu.

‡Commander, United States Navy, Assistant Professor, Department of Aerospace Engineering, 327B Rickover Hall; drayton@usna.edu.

Presented at the 43rd European Rotorcraft Forum, Milan, Italy 12–15 September 2017.

INTRODUCTION

The helicopter's relatively low forward flight speed has led to efforts to significantly increase its maximum speed. An important consideration for a high-speed helicopter is the utilization of a rotor system with high hovering efficiency and forward flight efficiency. However, designing to maximize the efficiency of one flight regime often requires degrading the efficiency of the other. One such design consideration is rotor blade twist. During hover, relatively high pitch angles and lift coefficients are required. Under these high-lift conditions the utilization of larger amounts of nose-down blade twist reduces the induced power requirements by producing a more uniform spanwise loading distribution (Ref. 1). However, on the advancing blade in high-speed cruise, lower blade pitch angles and lift coefficients are required. At high forward speeds, larger amounts of blade twist can result in reduced or negative lift production near the blade tip and degraded overall performance. Therefore, the blade twist utilized for the final rotor blade design is often significantly less than that what is required to maximize hover efficiency. As a result, there has been considerable interest in shape morphing or "smart" structures that alter the blade twist between hover and forward

flight regimes. A comprehensive review of shape morphing structure is provided by Barbarino et al. (Ref. 2). An alternative method for modifying the spanwise loading distribution in a manner similar to blade twist is the utilization of leading-edge protuberances.

The humpback whale (see Fig. 1), which features protuberances on the leading-edge of its pectoral flippers, was the inspiration for this investigation. Despite its large size, it has a small turning radius compared to other whale species (Ref. 4). Miklosovic et al. (Ref. 3) compared a scalloped and smooth (baseline) leading-edge flipper-like design and found a 40% increase in stall angle of attack, 6% increase in lift coefficient, and an increase in lift-to-drag ratio at pitch angles greater than the stall point of the baseline flipper. Wind turbines and tidal turbine blades have also used scalloped airfoil geometries to improve efficiency by mitigating blade stall effects in off-design conditions, such as gusty winds or slack tides (Refs. 5–7). Furthermore, a computational analysis of rotor blades with protuberances found that an increase in lift production was achieved within the stall region of the baseline blade, resulting in improved hovering efficiency (Ref. 8).

Previous studies suggest that protuberances improve an airfoils post-stall performance using a mechanism similar to vortex generators. Pedro and Kobayashi (Ref. 9) performed a computational study on an idealized model humpback whale flipper that showed the formation of streamwise vortices from the protuberances. They also found that the protuberances altered the vorticity distribution along the span of the model and increased the downstream vorticity. Experimental work performed by Hansen et al. (Ref. 10) and Hansen (Ref. 11) found that the strength of the vortices trailed from the protuberances was directly proportional to the angle of attack of the blade. Using passive vortex generators placed at an airfoil's leading-edge to model protuberances, Mai et al. (Ref. 12) found that the flow stayed attached at higher pitch angles but was only slightly influenced at lower angles. The vortex generators also reduced the magnitude of the nose-down pitching moment that occurred during dynamic stall. Therefore, protuberances could be beneficial in delaying the onset of steady and dynamic stall conditions.

Basic lifting line theory states that the bound circulation along a wing is directly related to the circulation trailed into the wake (Ref. 13). Therefore, the vortices trailed from the protuberances would be expected to affect the loading distribution along a rotor blade. Since protuberances have a small effect at low pitch angles (i.e., the advancing blade in forward flight) and a large effect at higher pitch angles (i.e., hovering flight), leading-edge protuberances would have the greatest effect on the distribution of bound circulation at high lift conditions. With proper understanding and design, protuberances may have the potential to passively modify the loading distribution along a rotor blade in a manner similar to blade twist.

The primary focus of previous studies on protuberances has been as a means of delaying the onset of stall (Refs. 3–10, 10–12, 14–22); however, there is a dearth of information on how protuberance amplitude and frequency affect the formation and strength of the streamwise vortices, and the effect these vortices have on the loading distribution of a rotor system. With this in mind, the goal of the present work was to examine the performance, wake structure, and trailed circulation generated by a rotor with protuberances.

Table 1: Summary of rotor characteristics and test conditions.

Number of Blades, N_b	2
Blade Radius, R	0.408 m (16 in)
Mean Chord, c	44.45 mm (1.75 in)
Thickness to Chord Ratio, t/c	15%
Rotational Frequency, Ω	35 Hz (2,100 RPM)
Blade Loading Coefficient, C_T/σ	0.12
Rotor Tip Speed, V_{tip}	89.1 $\mathrm{m\,s^{-1}}$ (292 $\mathrm{ft\,s^{-1}}$)
Tip Mach Number, $\mathrm{M_{tip}}$	0.27
Tip Reynolds Number, $\mathrm{Re_{tip}}$	280,000

DESCRIPTION OF THE EXPERIMENT

The experiment was conducted using a teetering two-bladed rotor system. Five sets of untwisted blades were tested, each with a radius of 0.408 m (16 in), mean chord of 44.45 mm (1.75 in), and NACA 0015 airfoil throughout. Flow field measurements were performed with each rotor configuration operating out of ground effect. A blade loading coefficient (C_T/σ) of 0.12 was selected to emphasize the effect the protuberances had on the rotor wake (discussed in detail in the Performance Measurements Section). The specific rotor characteristics and test conditions are outlined in Table 1.

Blade Design

Performance and flow field measurements were performed on four sets of blades with various sinusoidal leading-edges, as well as a baseline set of rectangular blades, as shown in Fig. 2. The amplitude and wavelength of the protuberances were selected based on prior experimental work by Johari et al. (Ref. 14). A schematic of protuberance dimensions are illustrated in Fig. 3. Sinusoidal amplitude, A, was measured from the mean chord line (i.e., the leading-edge of the baseline blade) to protuberance peak as a percentage of chord length, c. Wavelength, λ, was measured from peak to peak as a percentage of chord length. Amplitude effects were investigated using three amplitudes (A = $0.025c$, $0.05c$, and $0.12c$) with a constant wavelength $\lambda = 0.50c$. Wavelength effects were examined by varying wavelength ($\lambda = 0.25c$ and $0.50c$) and holding amplitude constant (A = $0.05c$). Table 2 shows the specific amplitudes and wavelengths examined, as well as the naming conventions used in the current work. Each blade was designed to maintain a constant mean chord length along the entire span of the blade, which yielded a thrust-weighted solidity ($\sigma_e = 3\int_0^1 \sigma r^2 dr$) of 0.0694 for each rotor.

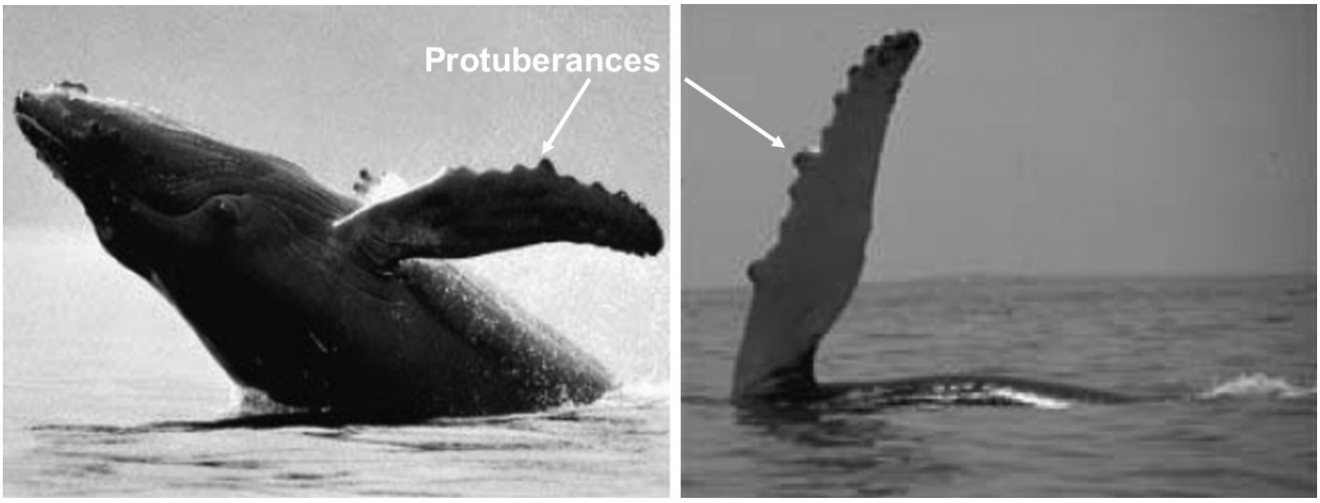

Fig. 1: Photograph of a Humpback whale's pectoral flippers with leading-edge protuberances (Ref. 3).

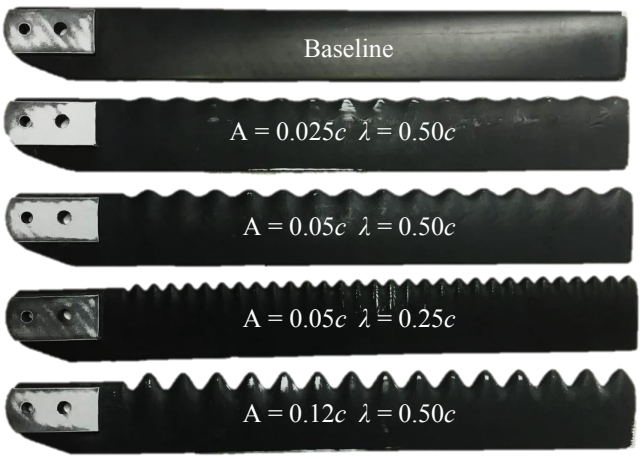

Fig. 2: Photograph of baseline and modified blades.

Performance Measurements

Performance sweeps were performed using a combination multi-axis load and torque cell. Tares were obtained by rotating the hub without the rotor blades attached, and these tares were removed from the performance sweeps. Performance sweeps for each blade set were obtained for collective pitches ranging from -2° to 18°. The accuracy of the cell was $C_T/\sigma = \pm 6.3 \times 10^{-5}$ and $C_P/\sigma = \pm 4.0 \times 10^{-6}$, respectively.

Table 2: Summary of geometric parameters for the baseline and modified blades.

Blade Designation	Amplitude, A	Wavelength, λ
Baseline	0	N/A
A025	0.025c	0.5c
A05	0.05c	0.5c
A05 HF	0.05c	0.25c
A12	0.12c	0.5c

Flow Field Measurements

Flow field measurements were performed using two-component particle image velocimetry (PIV). The configuration of the laser and camera is shown in Fig. 4. A thin light sheet was produced by firing the laser beam through a convex and spherical lens. The imaging axis of the camera was aligned orthogonal to the plane of the light sheet and focused on the desired region of interest (ROI). The camera and laser were digitally synchronized such that the laser pulses straddled the camera images.

Seeding Vaporizing a mineral oil in a high pressure head exchanger and mixing it with cooler ambient air produced the seed particles for the PIV measurements. Particle tracking errors were minimized by using seed particles approximately 0.22 μm in diameter (Ref. 23).

Phase-Resolved Flow Measurements One 29 mega-pixel CCD camera (6,600-by-4,400 pixel) and a dual-head Nd:YAG laser were used for the current flow field measurements. The laser was capable of emitting 532 nm light at 380 mJ/pulse when operated at a frequency less than or equal to 10 Hz in frame-straddling mode. The imaging system was synchronized with the rotational frequency of the rotor, since the rotor's rotational frequency (35 Hz) exceeded the maximum imaging rate of the camera (1.8 Hz). PIV images were only acquired at sub-integer multiples of the rotor frequency (i.e., one image approximately every 35 rotor revolutions).

PIV Imaging PIV measurements were conducted in a region encompassing a majority of the blade (approximately 370-by-250 mm, or 0.91-by-0.61 R), as shown in Fig. 5. The high-resolution camera was able to maintain the necessary resolution to resolve the small-scale vortical structures. Measurements were taken at blade azimuth increments of 3° from 0°

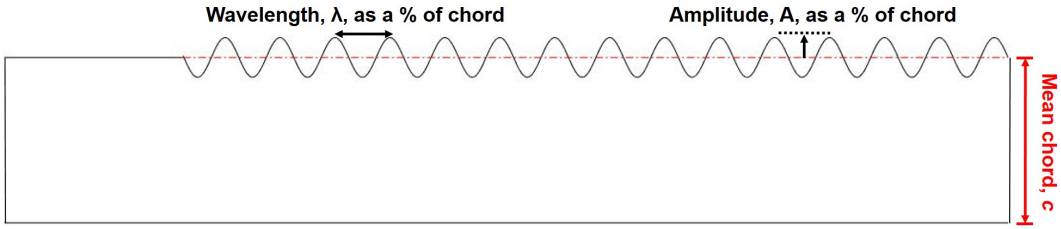

Fig. 3: Schematic showing protuberance amplitude and wavelength.

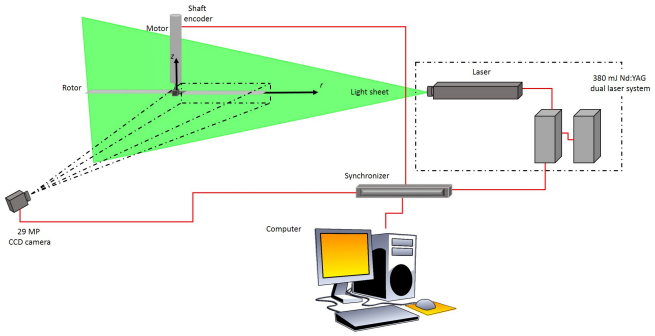

Fig. 4: Schematic showing the two-bladed rotor and the experimental setup with the laser and camera used for PIV.

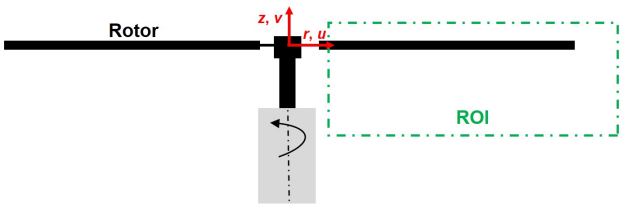

Fig. 5: Definition of the coordinate system and the region of interest used for the flow field measurements.

to 15° to examine the initial evolution of the trailed wake. Additional measurements were also taken from 0° to 150° in 30° increments. At each blade azimuth position, 300 image pairs were acquired using a pulse separation time of 18 μs.

The interrogation windows used for cross-correlation had dimensions of 32-by-32 pixels with a 75% overlap. The interrogation window size and shape was optimized to the local seeding density and flow field gradients using an adaptive grid method (Ref. 24). The adaptive method increased the spatial resolution while maintaining measurement accuracy. A local median filter was applied to the processed PIV data that removed vectors of greater than two standard deviations of the 5-by-5 neighboring vectors. Images containing more than 5% removed vectors were excluded from any further analysis.

RESULTS AND DISCUSSION

Performance Analysis

The blade loading coefficient, C_T/σ, versus power loading coefficient, C_P/σ, for each rotor configuration operating out of ground effect is shown in Fig. 6. Examining Fig. 6, the baseline and modified blades were found to have similar power requirements for $C_T/\sigma \leq 0.06$. As the blade loading coefficient was increased above 0.06, the modified blades began to incur an additional power penalty that was directly related to the protuberance amplitude. Comparing the power polar for the lowest and highest amplitude blades (see Fig. 6), the lowest amplitude blade begins to incur a power penalty at a C_T/σ approximately twice that of the highest amplitude blade. It is interesting to note that, while rotor performance was significantly affected by protuberance amplitude, changes in wavelength had a minimal effect. For additional performance analysis, see Cully et al. (Ref. 25).

For the subsequent flow field measurements the rotor was operated at a constant $C_T/\sigma = 0.12$. While most hovering rotors operate at blade loading coefficients around 0.08, the operating blade loading coefficient for the current work was selected such that all but the lowest amplitude blade had incurred a power penalty.

Time-Averaged Flow Field Measurements

Figure 7 shows contours of the "time-averaged" axial velocity for each rotor configuration, normalized by the blade tip speed, as well as the corresponding velocity vectors along various radial cuts through the rotor wake. Because the current measurements were phase-resolved, a time history could not be obtained. Therefore, the time-averaged flow field was generated by averaging each instantaneous realization at each blade azimuth position, ψ_b. To avoid biasing the average, only equally-spaced increments blade azimuth angles were used, i.e., $0° \leq \psi_b \leq 180°$ in 30° increments.

As shown in Fig. 7, each blade set produced a well-defined slipstream boundary, which separated the high-velocity flow inside the rotor wake from the quiescent flow outside the wake. As expected, the axial velocity distribution in the wake of the rotor with the baseline blades was biased towards the tip, with the highest velocities outboard and the lowest velocities inboard; see Fig. 7a. While the baseline and A025 (i.e., the lowest amplitude) blades produced relatively similar flow fields, the higher amplitude (i.e., A05, A05HF, and A12) blades increased the uniformity of the velocity distribution; see Fig. 7. Specifically, as protuberance amplitude increased the velocity distribution became more uniform.

From blade element momentum theory (BEMT) the power requirements should decrease as the velocity through the rotor

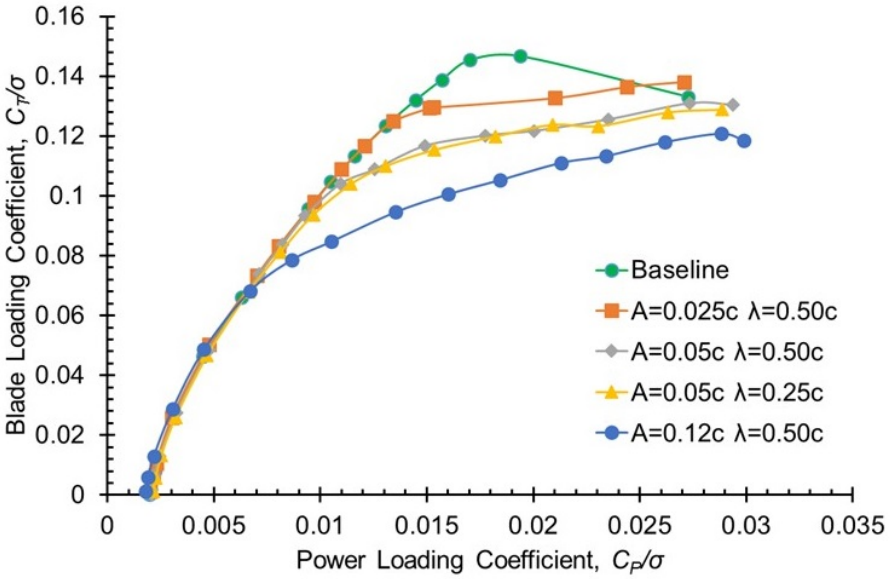

Fig. 6: Blade loading coefficient versus measured power loading coefficient for each rotor configuration (Ref. 25).

(i.e., the inflow) becomes more uniform (Ref. 1). However, the A012 blade produced the most uniform velocity distribution of the blades tested, and had the largest power requirements (see Fig. 6). Therefore, the power penalty associated with the modified blades would be expected to stem from a transient flow feature. One such flow feature could be the streamwise vorticies trailed from the protuberances.

Instantaneous Flow Field Measurements

Figure 8 shows representative contours of normalized instantaneous vorticity ($\omega c/\Omega R$) and the corresponding velocity vectors for each rotor configuration at a blade azimuth position of $\psi_b = 6^\circ$. To limit image congestion, only every 10th vector is displayed. Previous work has shown that the wake sheets trailed from a rotor blade consisted of counter-rotating vortex pairs (Refs. 26–28), often called Taylor–Görtler (T–G) vortices (Ref. 29). The T–G vortex pairs can be identified by the red (positive) and blue (negative) vorticity contours in Fig. 8, whereas the tip vortices appear as the larger regions of concentrated positive vorticity.

Comparing the wake sheets trailed from the A05 and A12 blades to the baseline and A025 blades, the wake sheet produced by the higher amplitude blades were significantly more intense; see Fig. 8. Specifically, the vortical structures in the sheets of the higher amplitude blades were of similar size and magnitude to that of the tip vortex. Furthermore, the tip vortices trailed from the larger amplitude blades was also less coherent, and persisted for less than one rotor revolution after interacting with the wake sheet. It is interesting to note that the most prominent vortices in the wake sheet produced by the modified blades were trailed outboard of $r/R \approx 0.70$, as shown in Fig. 8. Because power scales with the cube of radial position, the creation of relatively large vortical structures outboard on the blade would be expected to significantly effect the power requirements.

Milluzzo and Leishman (Ref. 27) showed that the addition of twist to a rotor blade significantly increased the vorticity trailed into the wake sheet, which was most likely caused by modifications to the spanwise distribution of bound circulation. With this in mind, the increased vorticity trailed from the blades with leading-edge protuberances suggests a potential modification to the spanwise distribution of bound circulation along the blades. Because the intensity of the wake sheets was directly related to the protuberance size, the blade with the largest amplitude would be expected to have the greatest effect on the distribution of bound circulation.

Wake Sheet Circulation

To further examine the effect leading-edge protuberances had on the rotor wake, it was necessary to quantify the circulation trailed into the wake sheet. One method for determining the circulation of a flow feature is through the evaluation of a line integral around a path enclosing the flow feature. For convenience, a square or rectangular grid is often utilized because it easily coincides with the PIV grid. However, the vortices in the wake sheet vary in size and shape, and are too closely spaced to define a path that encloses only the desired vortical element. Therefore, the current work used an area integral of voricity to calculate the circulation (Ref. 13). The vorticity was calculated using a 3-point central difference scheme, and the vortices were identified using a vorticity threshholding method. Specifically, the algorithm identified all points above the given vorticity threshold, and grouped the points into distinct vortices.

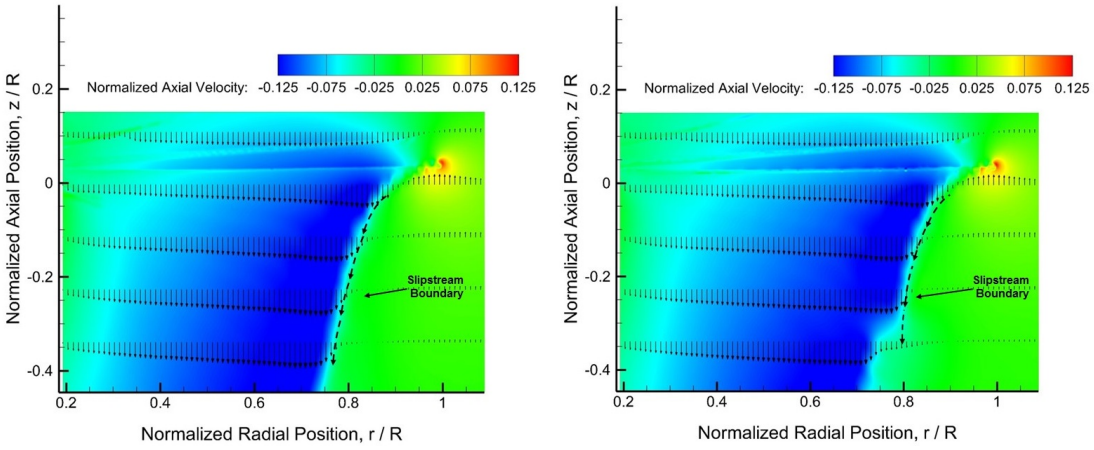

(a) Baseline Blade (b) A=0.025c λ=0.50c

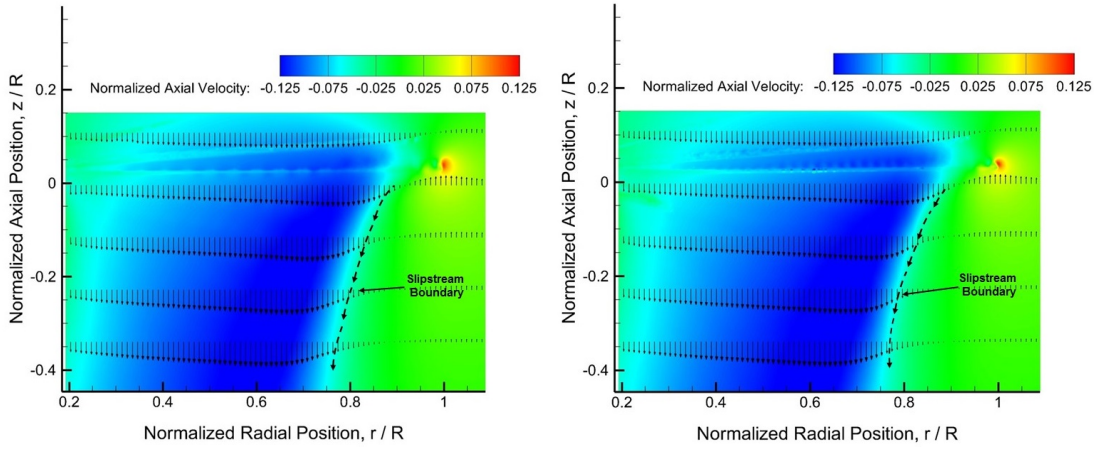

(c) A=0.05c λ=0.50c (d) A=0.05c λ=0.25c

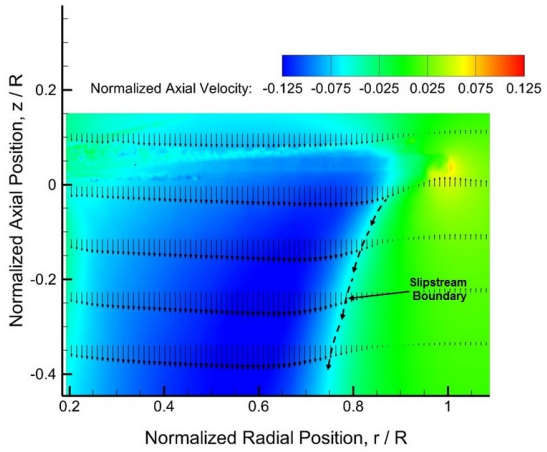

(e) A=0.12c λ=0.50c

Fig. 7: Time-averaged contours of axial velocity normalized by the rotor tip speed for each blade geometry (Ref. 25).

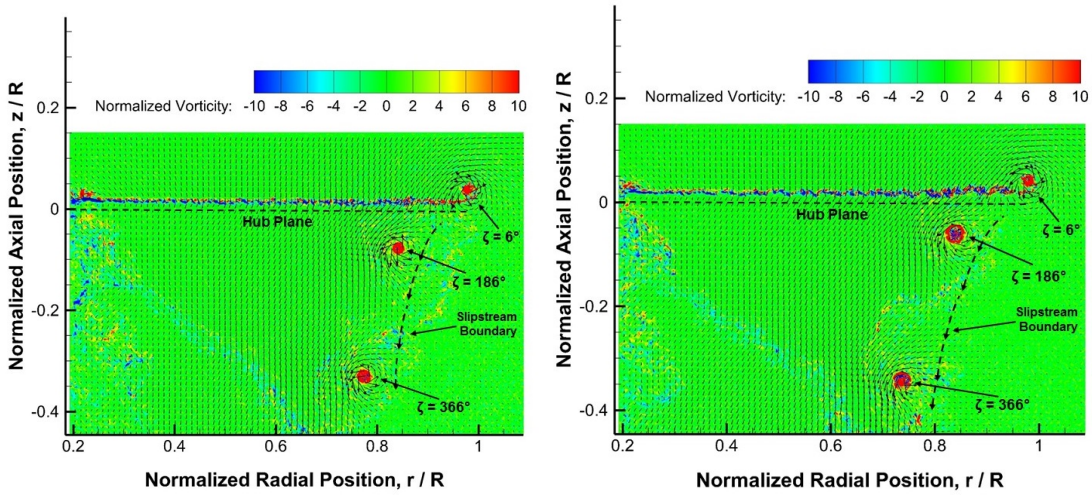

(a) Baseline Blade (b) A=0.025c λ=0.50c

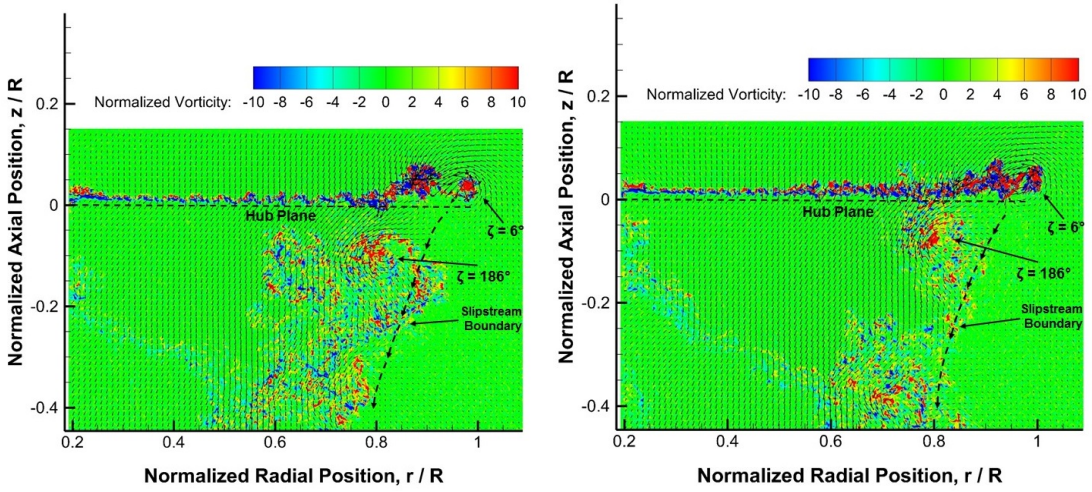

(c) A=0.05c λ=0.50c (d) A=0.05c λ=0.25c

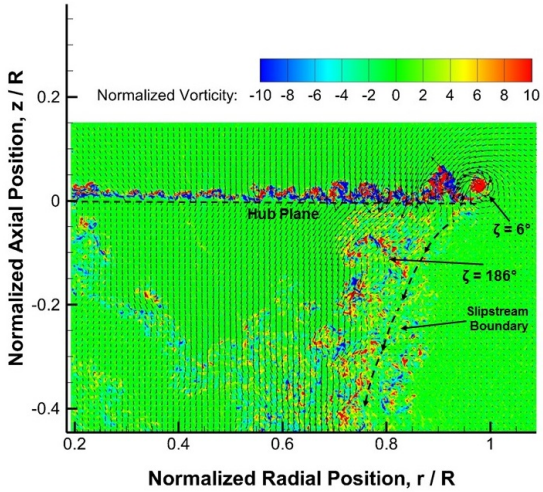

(e) A=0.12c λ=0.50c

Fig. 8: Instantaneous contours of normalized vorticty, with the reference blade at $\psi_b = 6°$. (Ref. 25).

The aperiodic nature of a rotor wake has been well documented and studied in detail (Refs. 30–33). Methods for collocating dominant flow structures (such as the tip vortices) to determine the average characteristics have been developed (Refs. 33–39). However, in the case of the wake sheet, which contains a broad spatial distribution of vorticity, such collocation techniques cannot be so easily applied. Therefore, average characteristics for the wake sheet, as in the manner that has been developed for tip vortices are difficult to acquire.

While the phase-averaged characteristics for a specific vortical element in the wake sheet cannot be determined, it was possible to determine the phase-averaged characteristics for all vortical elements at a specific radial location. Applying the previously described threshholding method to each flow field realization at a fixed wake age, it was possible to identify the size and position of each vortical element (both positive and negative vorticity) contained in the wake sheet. For each radial location, only realizations containing vortical elements were averaged. Therefore, the number of images used to obtain the average could vary with radial location. This process was repeated for each wake age, and for both signs of vorticity contained in the sheet.

Figure 9 shows the phase-averaged radial distribution of circulation trailed into the wake sheet for each blade at a wake age, ζ, of 6°. It is interesting to note that while both positive and negative vorticity (i.e., T-G vortices) were trialed into the wake sheet of the baseline blade, the negative vorticity was approximately three times stronger than the positive inboard of $r/R = 0.8$; see Fig. 9a. However, outboard of $r/R = 0.8$ the positive vorticity was stronger than the negative. Furthermore, spanwise distribution of both the positive and negative circulation trailed from the baseline blade remained relatively constant before reaching a peak and decreasing to zero, as shown in Fig. 9a. However, the radial position of the peak circulation was dependent on the sign of the circulation. Figure 9a shows that the negative circulation reached a peak at approximately $r/R = 0.8$ while the peak positive circulation occurred at approximately $r/R = 0.95$.

Compared to the baseline blade, the modified blades were found to significantly alter the circulation trailed into the wake sheet; see Fig. 9. Specifically, the modified blades produced a sinusoidal variation in the spanwise distribution of both the positive and negative circulation. The sinusoidal nature of the trailed circulation resulted in local circulation that was greater than or less than that of the baseline blade, as shown in Fig. 9. Examining Fig. 9, the amplitude of the sinusoidal variation of trailed circulation was directly related to protuberance amplitude, with the A12 blade trailing the strongest circulation. As compared to the baseline blade, the A05 and A12 blades also increased the magnitude of the mean circulation (both positive and negative) about which the sinusoidal oscillation occurred; see Fig. 9. Furthermore, the radial position at which the peak negative circulation occurred was also affected by the protuberances, with the negative circulation peaking at $r/R \approx 0.9$ as compared to $r/R \approx 0.8$ for the baseline blade.

CONCLUSIONS

To better understand the affect of leading-edge protuberances, performance and phase-resolved particle image velocitmetry measurements were conducted on a rotor operating out of ground effect. Protuberance amplitude and wavelength were examined using four sets of blades with various sinusoidal leading-edges, as well as a baseline set of rectangular blades. Emphasis was placed on characterizing the initial structure of the wake, as well as the circulation trailed into the wake sheet. From this work, the following conclusions have been obtained:

1. Protuberances were found to have a minimal effect on rotor performance for $C_T/\sigma \leq 0.06$. However, increasing rotor thrust requested in the modified blades requiring significantly more power than the baseline. The additional power requirements of the modified blades were directly related to protuberance amplitude. Whereas, wavelength was found to have minimal effect, with the higher and lower frequency blades having similar power requirements at all thrust conditions.

2. The time-averaged flow fields showed that protuberance amplitude affected the spanwise distribution of axial velocity (i.e., the inflow distribution). Specifically, increasing protuberance amplitude generated a more uniform inflow distribution. However, the average flow field was minimally affected by changes in protuberance wavelength.

3. The instantaneous flow fields showed that protuberance amplitude significantly affected the size and magnitude of the vorticity trailed into the wake sheet. The higher amplitude blades were found to produce significantly more intense wake sheets, with vortical elements of similar size and magnitude to that of the primary tip vortex. Furthermore, the tip vortices trailed from the higher amplitude blades were less coherent, persisting for less than one rotor revolution.

4. Protuberances were found to have a significant effect on the spanwise distribution of circulation trailed into the wake sheets. Specifically, a sinusoidal variation in both the positive and negative circulation distribution occurred for each of the modified blades. As compared to the baseline blade, the blades with the largest amplitude increased the magnitude of the mean circulation (both positive and negative) about which the sinusoidal oscillation occurred.

The current work has shown that protuberances are capable of significantly altering the wake trailed from a hovering rotor. Therefore, with proper design and optimization, protuberances could potentially be used to generate a desired loading distribution.

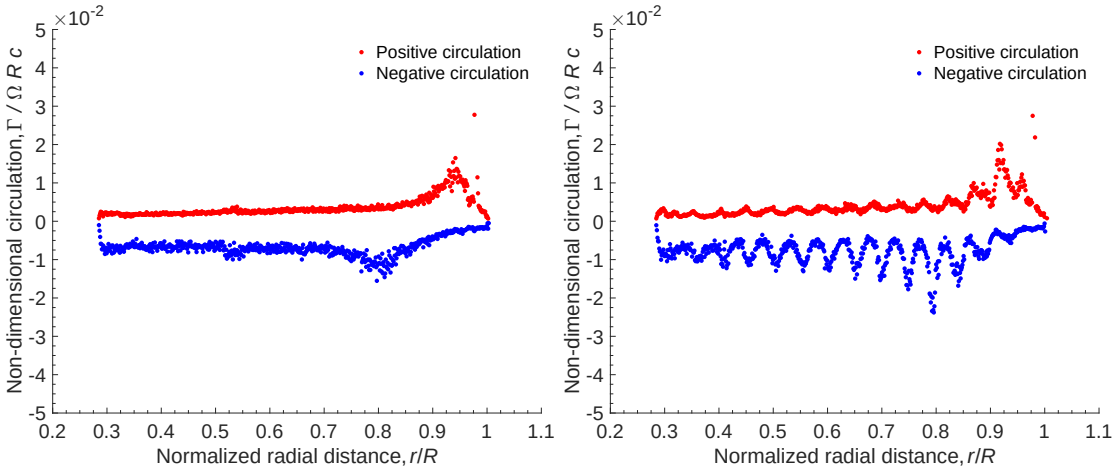

(a) Baseline Blade

(b) A=0.025c λ=0.50c

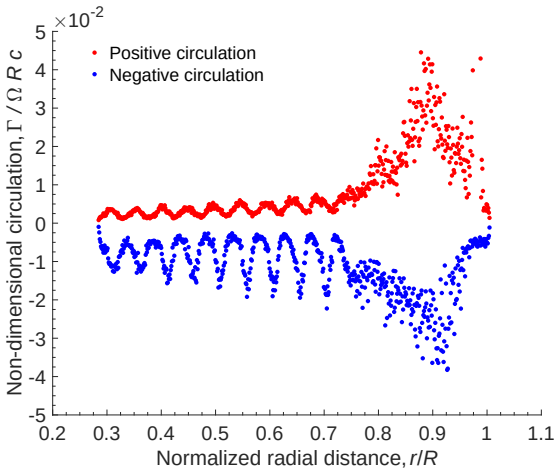

(c) A=0.05c λ=0.50c

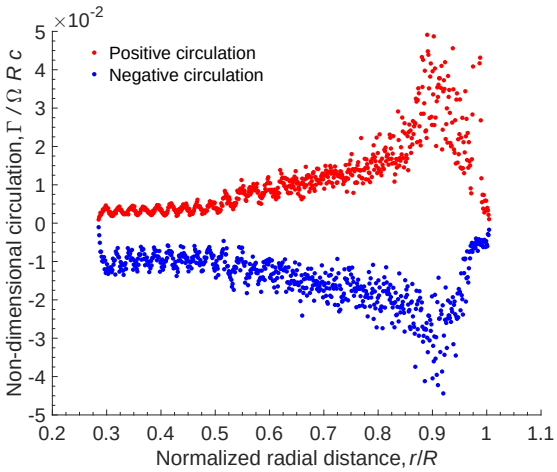

(d) A=0.05c λ=0.25c

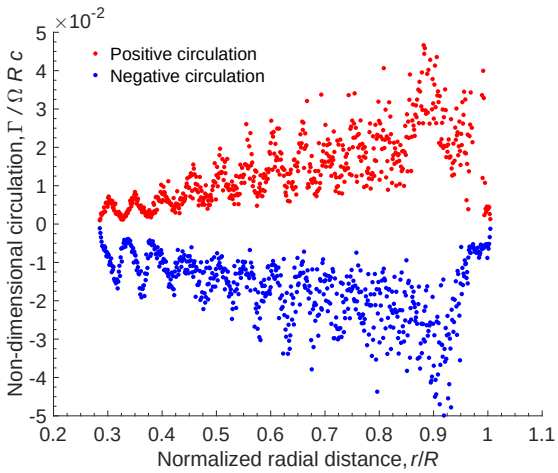

(e) A=0.12c λ=0.50c

Fig. 9: Phase-averaged plot of the spanwise distribution of trailed circulation contained in the wake sheet of each blade when the reference blade was at $\psi_b = 6^\circ$.

ACKNOWLEDGMENTS

Special thanks to Drs. David Miklosovic and Mark Murray for their support and guidance, and to Mr. Dan Rodgerson for his laboratory and experimental support.

REFERENCES

[1]Leishman, J. G., *Principles of Helicopter Aerodynamics*, Cambridge University Press, New York, NY, 2006.

[2]Barbarino, S., Bilgen, O., Ajaj, R. M., Friswell, M. I., and Inman, D. J.,, "A Review of Morphing Aircraft," *Journal of Intelligent Material Systems and Structures*, Vol. 22, (9), 2011, pp. 823–877.

[3]Miklosovic, D. S., Murray, M. M., Howle, L. E., and Fish, F. E., "Leading-Edge Protuberances Delay Stall on Humpback Whale (Megaptera novaeangliae) Flippers," *Physics of Fluids*, Vol. 16, (5), 2004, pp. 39–42.

[4]Fish, F. E., and Battle, J. M., "Hydrodynamic Design of the Humpback Whale Flipper," *Journal of Morphology*, Vol. 225, (1), 1995, pp. 51–60.

[5]Bai, C. J., Lin, Y. Y., Lin, S. Y., and Wang, W. C., "Computational Fluid Dynamics Analysis of the Vertical Axis Wind Turbine Blade with Protuberance Leading-Edge," *Journal of Renewable and Sustainable Energy*, Vol. 7, (3), 2015, pp. 033124.

[6]Zhang, R. K., Wu, J. Z., and Chen, S. Y., "A New Active Control Strategy for Wind-Turbine Blades under Off-Design Conditions," *International Journal of Modern Physics*, Vol. 19, 2012, pp. 283–292.

[7]Bolzon, M. D., Kelson, R. M., and Arjomandi, M., "Tubercles and Their Applications," *Journal of Aerospace Engineering*, Vol. 29, (1), 2015, pp. 04015013.

[8]"CFD Analysis of Novel Biomimetically Inspired Helicopter Rotor Geometries," Technical Report 0117059, Sikorsky Aircraft Corp., October 2011.

[9]Pedro, H. T. C., and Kobayashi, M. H., "Numerical Study of stall Delay on Humpback Whale Flipper," Paper AIAA-90-3008, Proceedings of the 46th AIAA Aerospace Sciences Meeting and Exhibit, January 7–10, 2008.

[10]Hansen, K. L., Kelso, R. M., and Dally, B. B., "Performance Variations of Leading-Edge Protuberances for Distinct Airfoil Profiles," *AIAA Journal*, Vol. 49, (1), 2011, pp. 185–194.

[11]Hansen, K. L., *Effect of Leading-Edge Tubercles on Airfoil Performance*, Ph.d. dissertation, Department of Mechanical Engineering, University of Adelaide, Adelaide, Australia, 2012.

[12]Mai, H., Dietz, G., Geiler, W., Richter, K., Bosbach, J., Hugues, R., and de Groot, K., "Dynamic Stall Control by Leading-Edge Vortex Generators," *Journal of the American Helicopter Society*, Vol. 53, (1), 2008, pp. 26–36.

[13]Anderson, J. D., *Fundamentals of Aerodynamics*, Mcgraw-Hill Companies Inc., New York, NY, 2005.

[14]Johari, H., Henoch, C., Custodio, D., and Levshin, A., "Effects of Leading-Edge Protuberances on Airfoil Performance," *AIAA Journal*, Vol. 45, (11), 2007, pp. 2634–2642.

[15]van Nierop, E. A., Alben, S., and Brenner, M. P., "How Bumps on Whale Flippers Delay Stall: an Aerodynamic Model," *Physical Review Letters*, Vol. 100, (5), 2007, pp. 054502.

[16]Miklosovic, D. S., Murray, M. M., and Howle, L. E., "Experimental Evaluation of Sinusoidal Leading-Edges," *Journal of Aircraft*, Vol. 44, (4), 2007, pp. 1404–1407.

[17]Stein, B., and Murray, M. M., "Stall Mechanism Analysis of Humpback Whale Flipper Models," Paper AIAA-90-3008, Proceedings of Unmanned Untethered Submersible Technology (UUST), January, 2005.

[18]Fish, F. E., Weber, P. W., Murray, M. M., and Howle, L. E., "The Tubercles on Humpback Whales Flippers: Application of Bio-Inspired Technology," *Integrative and Comparative Biology*, Vol. 51, (1), 2011, pp. 203–213.

[19]Murray, M. M., "Effects of Leading-Edge Protuberances on a Representative Whale Flipper Model at Various Sweep Angles," Proceedings of the 14th International Symposium on Unmanned Untethered Submersible Technology, August, 2005.

[20]Zhang, R. K., and Wu, J. Z., "Aerodynamic Characteristics of Wind Turbine Blades with a Sinusoidal Leading-Edge," *Wind Energy*, Vol. 15, (3), 2012, pp. 407–424.

[21]Gruber, T., Murray, M. M., and Fredriksson, D. W., "Effect of Humpback Whale Inspired Protuberances on Marine Tidal Turbine Blades," ASME 2011 International Mechanical Engineering Congress and Exposition, 2011.

[22]Dropkin, A., Custodio, D., Henoch, C. W., and Johari, H., "Computation of Flowfield Around an Airfoil with Leading-Edge Protuberances," *Journal of Aircraft*, Vol. 49, (5), 2012, pp. 1345–1355.

[23]Leishman, J. G., "On Seed Particle Dynamics in Tip Vortex Flows," *Journal of Aircraft*, Vol. 33, (4), 1996, pp. 823–825.

[24]Scarano, F., "Iterative Image Deformation Methods in PIV," *Measurement Science and Technology*, Vol. 13, (1), 2002, pp. R1–R19.

[25]Cully, B., Milluzzo, J., and Drayton, S., "PIV Flow Field Measurements of Hovering Rotors with Leading-Edge Protuberances," 73th Annual Forum Proceedings of the American Helicopter Society, May 9–11, 2017.

[26]Ramasamy, M., Johnson, B., and Leishman, J. G., "Tip Vortex Measurements using Dual Plane Digital Particle Image Velocimetry," American Helicopter Society 64th Annual Forum Proceedings, April 29–May 1, 2008.

[27]Milluzzo, J., and Leishman, J. G., "Fluid Dynamics of the Helicoidal Wake Sheets Trailed from a Hovering Rotor," *Journal of the American Helicopter Society*, Vol. 61, (1), January 2016, pp. 1–17.

[28]Milluzzo, J., and Leishman, J. G., "Vortical Sheet Behavior in the Wake of a Rotor in Ground Effect," *AIAA Journal*, Vol. 55, (1), January 2017, pp. 24–35.

[29]Hall, P., "Taylor–Görtler Vortices in Fully Developed Boundary Layer Flows," *Journal of Fluid Mechanics*, Vol. 124, (3), 1982, pp. 475–494.

[30]Leishman, J. G., "Measurements of the Aperiodic Wake of a Hovering Rotor," *Experiments in Fluids*, Vol. 25, (4), September 1998, pp. 352–361.

[31]Leishman, J. G., Martin, P. B., and Pugliese, G., "High Resolution Trailing Vortex Measurements in the Wake of a Hovering Rotor," *Journal of the American Helicopter Society*, Vol. 48, (1), 2003, pp. 39–52.

[32]McAlister, K., "Rotor Wake Development During the First Revolution," *Journal of the American Helicopter Society*, Vol. 49, (4), October 2004, pp. 371–390.

[33]Ramasamy, M., Johnson, B., Huismann, T., and Leishman, J. G., "Digital Particle Image Velocimetry Measurements of Tip Vortex Characteristics Using an Improved Aperiodicity Correction," *Journal of the American Helicopter Society*, Vol. 54, (1), 2009, pp. 1–13.

[34]Takahashi, R. K. and McAlister, K. W., "Preliminary Study of a Wing-Tip Vortex Using Laser Velocimetry," Technical Report 88,343, NASA TM, January 1987.

[35]Yamauchi, G. K., Burley, C. L., Mercker, E., Pengel, K., and Janakiram, R., "Flow Measurements of an Isolated Model Tilt Rotor," Proceedings of the 55th Annual American Helicopter Society Forum, May 2527, 1999.

[36]Ramasamy, M., and Bhagwat, M. J., "Effect of Tip Vortex Aperiodicity on Measurement Uncertainty," *Experiments in Fluids*, Vol. 53, (5), July 2012, pp. 11911202.

[37]van der Wall, B. G., Burley, C. L., Yu, Y., Richard, H., Pengel, K., and Beaumierf, P., "The HART II Test Measurement of Helicopter Rotor Wakes," *Aerospace Science and Technology*, Vol. 8, (4), June 2004, pp. 273–284.

[38]van der Wall, B. G., and Richard, H., "Analysis Methodology for 3C PIV Data of Rotary Wing Vortices," *Experiments in Fluids*, Vol. 40, (5), May 2006, pp. 798–812.

[39]van der Wall, B. G., and Schneider, O., "Conditional Averaging Methodology for Periodic Data with Time Jitter and Spatial Scatter," Proceedings of the 33rd European Rotorcraft Forum, September 11-13, 2007.